LEADING EDGE VORTEX FLOW OVER A 75 DEGREE-SWEPT DELTA WING- EXPERIMENTAL AND COMPUTATIONAL RESULTS*

ICAS-86-1.5.1

R. Carcaillet, F. Manie, D. Pagan, J.L. Solignac
Office National d'Etudes et de Recherches Aérospatiales
BP 72 - 92322 Châtillon Cedex, France

Abstract

A detailed experimental investigation of the leading edge vortex flow over a 75°-swept, sharp-edged delta wing set at an angle of attack $\alpha = 20°$ is reported. It has been conducted in several ONERA wind tunnels and involved flowfield surveys using a five-hole pressure probe and LDV techniques. Reynolds number effects are evidenced, and the structure of the vortical flow regions is discussed : they are shown to be of non-conical nature.

Global and local experimental data is then used to assess the 3-D vortex particle method being developed at ONERA. Recent improvements to the method are presented. Various test cases demonstrate its capabilities ; in particular, computation of the vortex flow over a 70°-swept delta wing at $\alpha = 20°$ leads to a remarkably good agreement with results obtained from other methods.

I. Introduction

The vortex flow that occurs at the swept leading edges of slender wings plays an essential role in the high-angle-of-attack aerodynamics of fighter aircrafts and missiles. Improving the knowledge of such flows as well as developing computational methods for predicting them have long been research topics of interest[1-4]. The non-conical, complex structure of the leading edge vortex flow over slender wings is more and more clearly evidenced by three-dimensional measuring techniques.

While increasing computer power now allows the development of computational methods able to predict a complete three-dimensional vortical flowfield, their assessment obviously requires detailed experimental data for a basic wing configuration. Consequently, the Aerodynamics Department at ONERA recently conducted fundamental experimental investigations of the sharp leading edge vortex flow over a 75°-swept delta wing model at an angle of attack $\alpha=20°$; such delta wings of A.R. $\simeq$ 1 have been considered in many studies so far[5-7]. The experiments involved usual oil flow visualizations and pressure measurements at the wall as well as more advanced techniques : flowfield surveys using a five-hole pressure probe, three-dimensional flow visualizations and LDV measurements.

These tests were performed for a large range of freestream Reynolds numbers, providing information in both the laminar and the turbulent flow cases. The corresponding results are discussed in the first part of this paper. Emphasis is put on the topology of the vortical flowfield through a detailed description of the mean physical quantities and of their fluctuations.

On the other hand, the three-dimensional vortex particle method developed at ONERA already provided encouraging results on various wing planforms for both steady and unsteady flows[8-11]. Improvements of the method have been recently tested for the prediction of leading edge vortex flow over the 75°-swept delta wing. Therefore, comparisons are presented between experimental and computational results in the second part of this paper.

Further comparisons deal with the leading edge vortex flow over a 70°-swept delta wing, for which computational results are available from the VORSEP free vortex sheet method and from an Euler code[12].

Nomenclature

b	local semispan
c	chord length
C_p	static pressure coefficient
C_{p_t}	total pressure coefficient
Re_c	Reynolds number $Re_c = \frac{V_o\, c}{\nu}$
Re_x	Reynolds number $Re_x = \frac{V_o\, x}{\nu}$
$\vec{V}$	velocity vector
u,v,w	mean velocity components
V_o	freestream velocity
X,Y,Z	wind tunnel coordinates
x	wing chordwise coordinate
α	angle of attack
Ω	vorticity magnitude
Ω_X	streamwise vorticity $\Omega_X = \frac{c}{V_o}\left(\frac{\partial w}{\partial Y} - \frac{\partial v}{\partial Z}\right)$

II. Experimental Investigation

II.1. Experimental Set-up

Experimental investigation of the flow over a 75°-swept, sharp-edged delta wing has been carried out in three different wind tunnels. Their respective features and equipment, specified in Figure 1, allowed the gathering of complementary experimental data. Two models have been used, consisting of a flat plate with leading edges beveled off at 20° on the lower surface. One model having a chord length $c = 1.45$ m and 247 pressure holes has been studied in the two largest wind tunnels (F1 and F2). The other model having a chord length $c = 0.5$ m has been studied in the S2LCh-wind tunnel.

* This work was partly supported by the S.T.P.A. (Service Technique des Programmes Aéronautiques) of the French Defence Ministry.

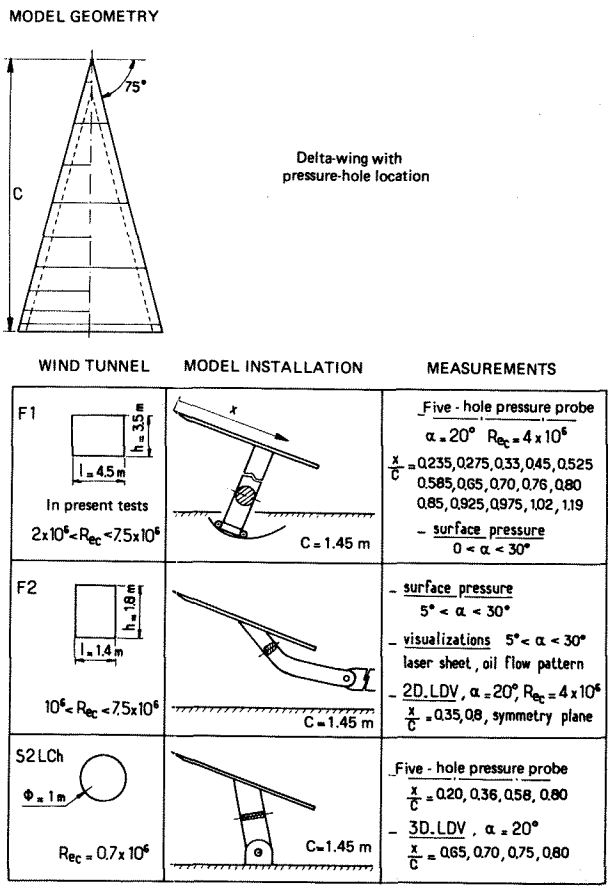

Figure 1. Model definition and test conditions.

The F1 subsonic pressurized wind tunnel uses the flowfield investigation methods which have been developed at ONERA for large wind tunnels[13]. They are based on the computer-controlled motion of a motorized exploring device[14]. In the case of the large delta wing model tests, the latter generates plane surfaces along the wing chord which are perpendicular to the freestream velocity. Measurements are made using a five-hole pressure probe that provides mean values of the velocity vector as well as local static and total pressure coefficients.

These surveys are performed at a freestream velocity V_o = 40 m.s^{-1}. The corresponding free-stream Reynolds number (c = 1.45 m) is Re_c = 4 10^6.

The F2 wind tunnel, a detailed description of which can be found in reference [15], is well suited for laser velocimetry. Its velocimeter is identical in its operating principles with the one used at S2LCh, but is permanently installed on a test section especially designed to receive it. For the present test, it performs 2-D measurements of the longitudinal (u) and vertical (w) velocity components.

The S2LCh wind tunnel is a smaller research facility that allows the use of the ONERA 3-D laser velocimeter[16]. This apparatus, schematically represented in Figure 2, is a 3 colour velocimeter used here in the forward scattering mode. The blue and green beams emitted by one argon laser are first split and then focused on the measurement point, where two patterns of horizontal and vertical fringes form in a (X,Z)-plane. The violet beam, emitted by a second laser, is also split and focused on the measurement point to form a third pattern of vertical fringes in a plane inclined at 55° to the preceding plane. The measurement point is observed by two Cassegrain telescopes located on the other side of the test section. One of them extracts the blue and green components of the scattered light, the other one the violet component. Three photomultipliers are associated with DISA counters connected to a minicomputer which performs data acquisition and processing, giving the various statistical quantities of the flow. This computer also drives the displacements of the XYZ benches on which the emitting and collecting modules of the velocimeter are mounted.

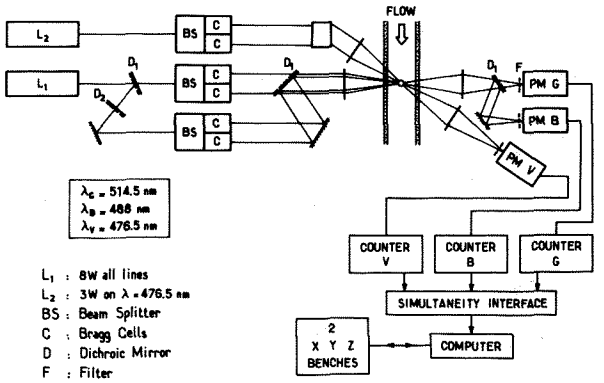

Figure 2. Scheme of ONERA 3-D laser velocimeter.

II.2. General Features of the Flow - Visualizations

Figure 3 presents visualizations of skin-friction lines, obtained by an oil flow technique at an incidence α=20° for three values of the freestream Reynolds number in the F2 wind tunnel. The conjectural streamline pattern is shown in Figure 4 in a plane normal to the wing surface : it agrees with the visualization. This pattern is characterized by the existence of a first separation point S1, origin of the vortex sheet which, by rolling up around the focus F1, constitutes the primary vortex. A second separation point S2 is clearly visible. The vortex sheet originating at S2 is rolling up around the second focus F2. A third separation line seems to be detected by surface visualizations (Figure 3.c). It leads to the existence of a third focus F3. Topological reasons imply the existence of three reattachment points A1, A2, A3 on the upper surface of the wing. A1, located in the symmetry plane, is the only one to be clearly visible in Figures 3.a to 3.c. The reattachment point A2 is probably located very close to the leading edge and its location is in fact almost identical with that of S1. A saddle singular point C1 is present in the outer flow far above the upper surface (see visualizations, Figure 9.b). The flow on the lower surface has not been visualized ; the streamline pattern presented in Figure 4 with an

attachment point A4 results from symmetry conditions. It is worth noting that the number of singular points which include 3 foci (F1, F2, F3) and 8 half-saddle points (S1,S2, S3, A1, A2, A3, A4, C1) satisfies the topological rule :

$$(\Sigma \text{ nodes} + \frac{1}{2} \Sigma \text{ half-nodes}) = (\Sigma \text{ saddle} + \frac{1}{2} \Sigma \text{ half-saddle}) - 1,$$

knowing that foci and nodes are topologically equivalent[2,17].

Wall streamline visualizations, made on the 1.45 m chord model, also show the effect of the nature of the upper surface boundary-layer. In Figure 3.a, obtained for $Re_c = 0.7\ 10^6$, the boundary-layer is laminar over the entire upper surface and the S2 line is located at Y/b = 0.71. For a higher Reynolds number ($Re_c = 2.5\ 10^6$, Figure 3.b), transition occurs near the half chord of the wing. In this case the secondary separation line S2 bends and is located at Y/b = 0.8 in the turbulent zone. For $Re_c = 4.1\ 10^6$, transition has moved up into the forward quarter of the wing and velocities are now high enough to evidence the separation line S3, which is approximately located at Y/b = 0.91 (Figure 3.c).

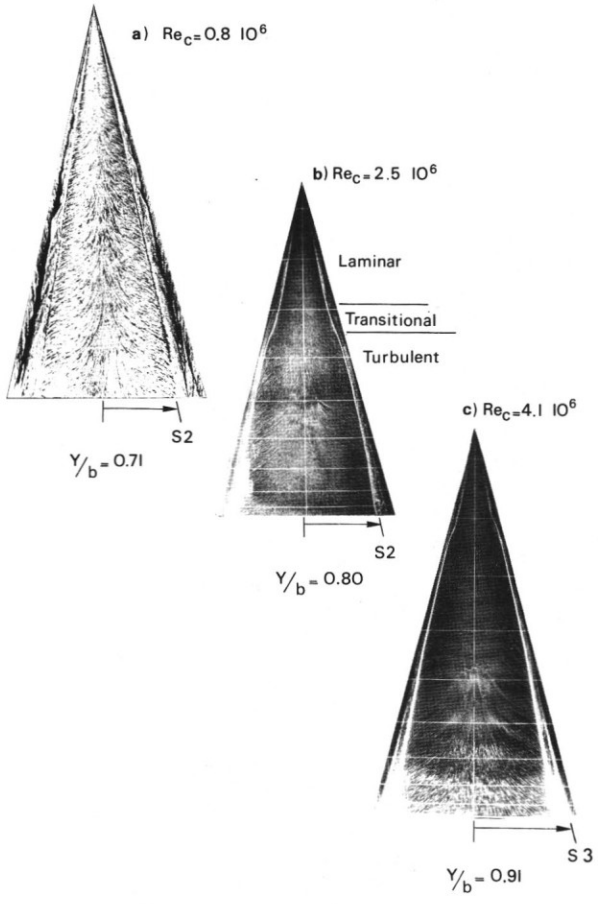

Figure 3. Oil flow patterns on the wing upper surface, α = 20°.

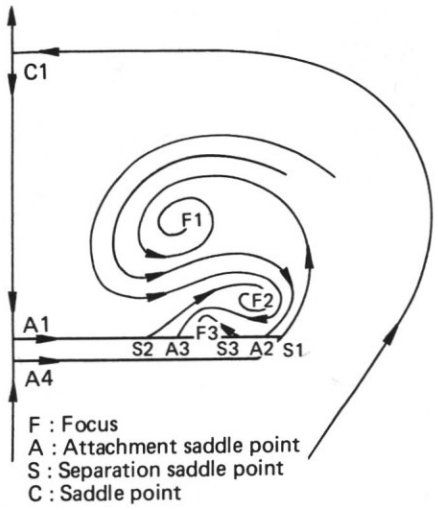

Figure 4. Schematic representation of the flow structure in a plane normal to the wing.

Figure 5 presents static pressure contours on the upper surface of the wing at an incidence α=20° for increasing values of the freestream Reynolds number. In the laminar flow case (Figure 5.a), the depression that appears under the primary vortex gives rise to a minimum pressure coefficient $C_{p_{min}} = -1.72$. The low pressure area almost reaches the leading edge. As the Reynolds number increases, we first observe a stronger pressure decrease in the laminar region and a secondary minimum appears downstream of the transition zone ; $C_{p_{min}}$ reaches -2.06 for $Re_c = 5.2\ 10^6$. This secondary minimum progressively moves up towards the apex.

Beyond $Re_c = 5.2\ 10^6$, on the other hand, the flow structure does not change significantly as the Reynolds number increases.

These phenomena can be explained by considering Figure 6, which displays spanwise surface pressure distributions for two Reynolds number values : one corresponding to a laminar boundary-layer ($Re_x = 0.54\ 10^6$), the other one to a turbulent boundary-layer ($Re_x = 4\ 10^6$). The approximate positions of the primary and secondary vortices are shown in the same figure, as determined by laser sheet visualizations. In the laminar case, the separated zone is wider and originates close to the primary vortex axis. Thus, it tends to reduce the pressure decrease induced on the upper surface of the wing by the primary vortex and to smooth out the pressure up to the leading edge. In the turbulent case, we observe an important suction peak induced by the primary vortex ; the secondary separation line is located closer to the leading edge.

With the help of flow visualizations and surface pressure measurements, we were able to locate the transition zone. Its extent has been characterized by the respective locations of the end of the purely laminar boundary-layer and that of the beginning of fully turbulent flow. The Reynolds numbers calculated with the distance between the apex and the two points considered have been plotted in Figure 7.

The mean location of transition ranges from $Re_x = 1.5\ 10^6$ for $\alpha=10°$ to $Re_x = 0.95\ 10^6$ for $\alpha=30°$, its evolution being monotonous and the extent of the transition zone decreasing as the incidence increases. The curve obtained by Hummel[6] for a wing of aspect ratio AR=1, that gives the end of the laminar zone, has also been drawn in Figure 7.

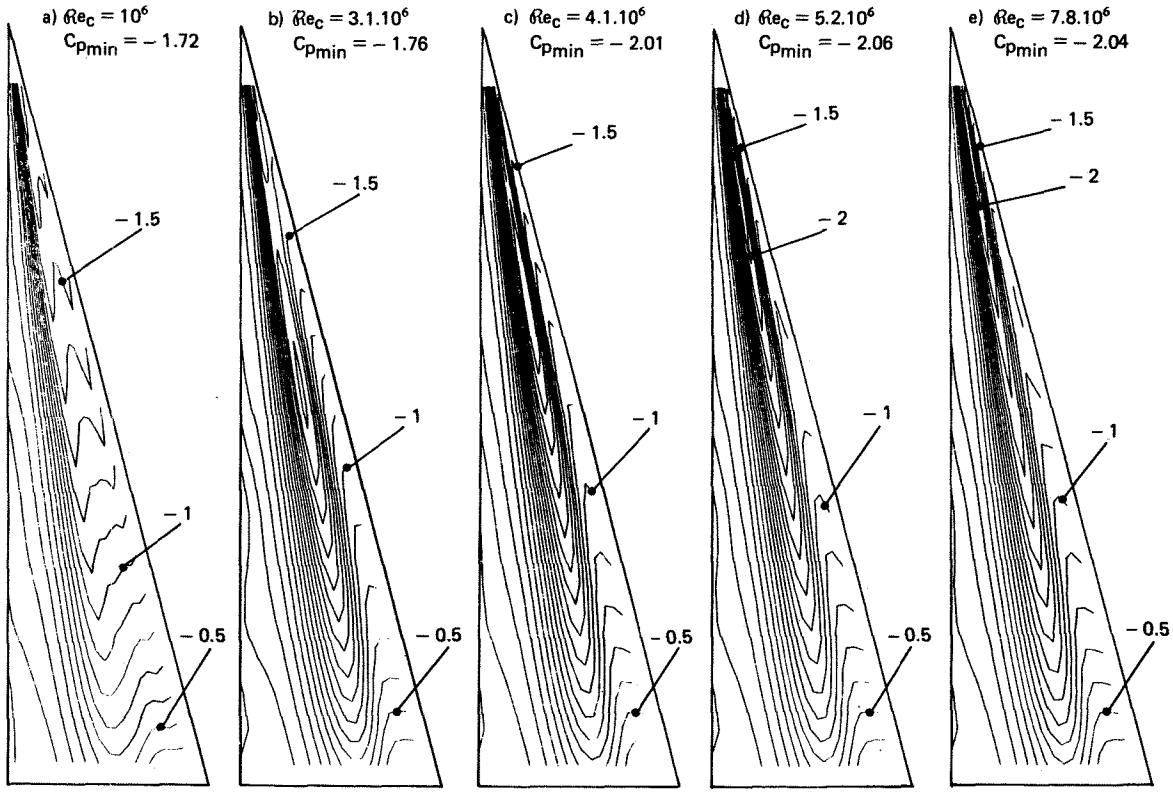

Figure 5. Isobar patterns on the wing upper surface, $\alpha = 20°$, $\Delta C_p = 0.1$.

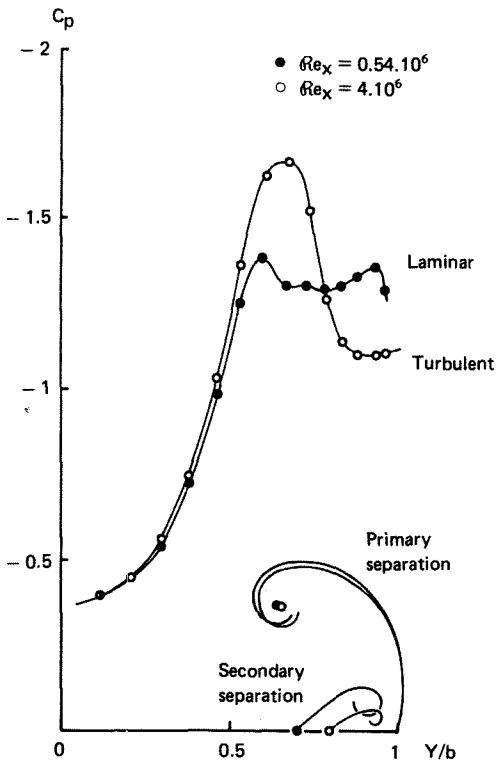

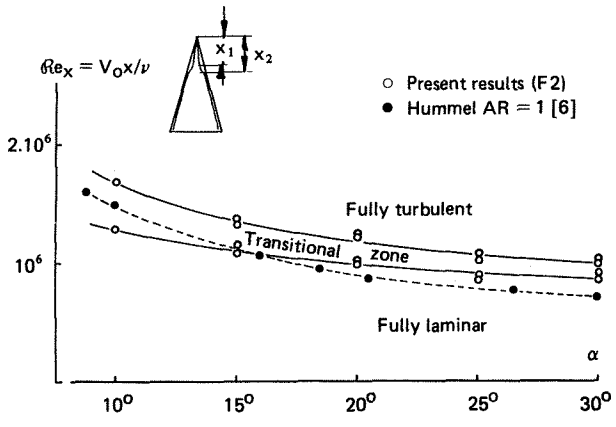

Figure 7. Influence of angle of attack on transition location.

◀ *Figure 6. Reynolds number effect on spanwise upper surface pressure distribution, $\alpha = 20°$.*

Flowfield visualizations using laser sheets allow us to determine the location of the primary vortex axis in a vertical plane. In Figure 8 are plotted the reduced coordinates Y/b and Z/b of this axis for several incidence and Reynolds number values. At constant Reynolds number, the vortex is rapidly moving away from the wing as the incidence increases, while its spanwise coordinate Y/b remains almost constant. On the other hand, with present results (F2 wind tunnel, Figure 8.a), it seems more difficult to characterize the evolution of vortex location as Re_c varies. Nevertheless, taking into consideration Werlé's results[5] for lower Reynolds numbers, it clearly appears that the vortex moves closer to the leading edge as Re_c increases. This effect vanishes for high Reynolds numbers ($Re_c > 10^6$). Figure 8.b shows that at constant Reynolds number and incidence, the primary vortex location is the same in the sections $\frac{x}{c} = 0.28$ and $\frac{x}{c} = 0.80$; that is consistent with the hypothesis of conical geometry of the primary vortex.

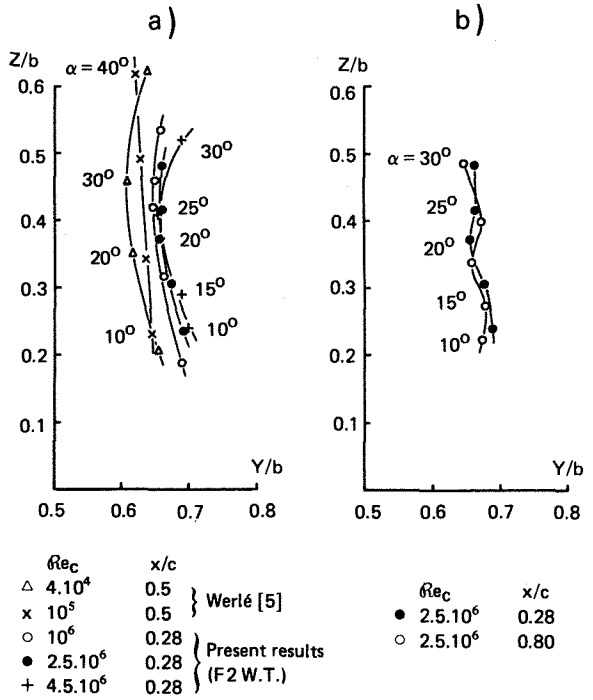

Figure 8. Location of primary vortex axis : a) Influence of angle of attack and Reynolds number, b) Variation of location with angle of attack and distance from the apex.

II.3. Study of the Mean Velocity Field

The results presented here have been obtained in the S2LCh wind tunnel for $Re_c = 0.7\ 10^6$, by means of five-hole pressure probe measurements and 3-D laser velocimetry.

Figure 9 compares a water tunnel visualization obtained by Werlé, on which the secondary vortex is particularly visible, with a vector plot of the mean velocity projection in a plane normal to the freestream velocity V_o, deduced from wind tunnel measurements. At each measuring point P of the plane, the projection of the velocity vector has been performed along a direction defined by the line AP, where A is the apex of the wing. In this way, for conical flow, the vectors in the projection plane seem to be tangential to the lines displayed by the visualizations.

Figure 10 shows two kinds of representations that give an idea of the extent of the rotational regions. These representations are total pressure contours, on one hand, and contours of the streamwise vorticity component, on the other hand. These results are given for $\frac{x}{c} = 0.6$ (laminar and turbulent cases). Still, such an increase in Reynolds number does not lead to fundamental changes in the separated flow region :

- as sketched in Figure 6, both the primary and the secondary vortices slightly move towards the leading edge ; the secondary vortex clearly decreases in size and moves closer to the wall ;

- the slight decrease in total pressure loss and streamwise vorticity component observed near the axis of the primary vortex is not necessarily significant.

Figure 11 shows, in four different chordwise sections, the pressure and velocity distributions for vertical traverses passing through the primary vortex core. In order to let these distributions coïncide far from the wing ($Z/b > 1$), we had to multiply each set of values by a certain coefficient "CD".

The evolution of these coefficients is given in Figure 12, which allows us to determine the departure of the actual flow from conical flow, for which all of these coefficients would be equal to 1. Here, the coefficients monotonously increase along the chord. While they remain relatively close to 1 for the velocity components (1.15 is the maximum value), they reach 1.4 for the static and total pressures.

Therefore, it seems necessary to take into account the three-dimensional effects in order to get a good representation of the actual pressures and velocity.

II.4. Turbulent Field Survey

Measurements carried out at S2LCh using 3-D laser velocimetry allow us to obtain the six components of the Reynolds stress tensor. They are represented in Figures 13 and 14 at the section $\frac{x}{c} = 0.6$.

First of all, it is worth noting the high turbulence level in the three following regions : primary vortex, separated region, and leading edge vortex sheet. In these regions, the RMS values $\sqrt{\overline{u'^2}}$, $\sqrt{\overline{v'^2}}$ and $\sqrt{\overline{w'^2}}$ most often exceed 0.2 V_o, and values as high as 0.3 V_o are found in the leading edge vortex sheet.

The large values measured near the wall in the vicinity of the secondary separation point ($\sqrt{\overline{v'^2}}/V_o \simeq 0.2$) where the boundary-layer is laminar can be explained only by the instability of the separation line location.

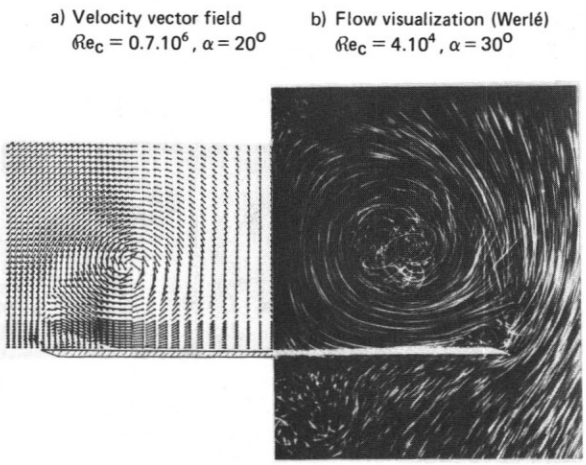

Figure 9. Laminar transverse flowfield :
a) velocity vector field $Re_c = 0.7\ 10^6$, $\alpha = 20°$
b) flow visualization (Werlé) $Re_c = 4\ 10^4$, $\alpha = 30°$.

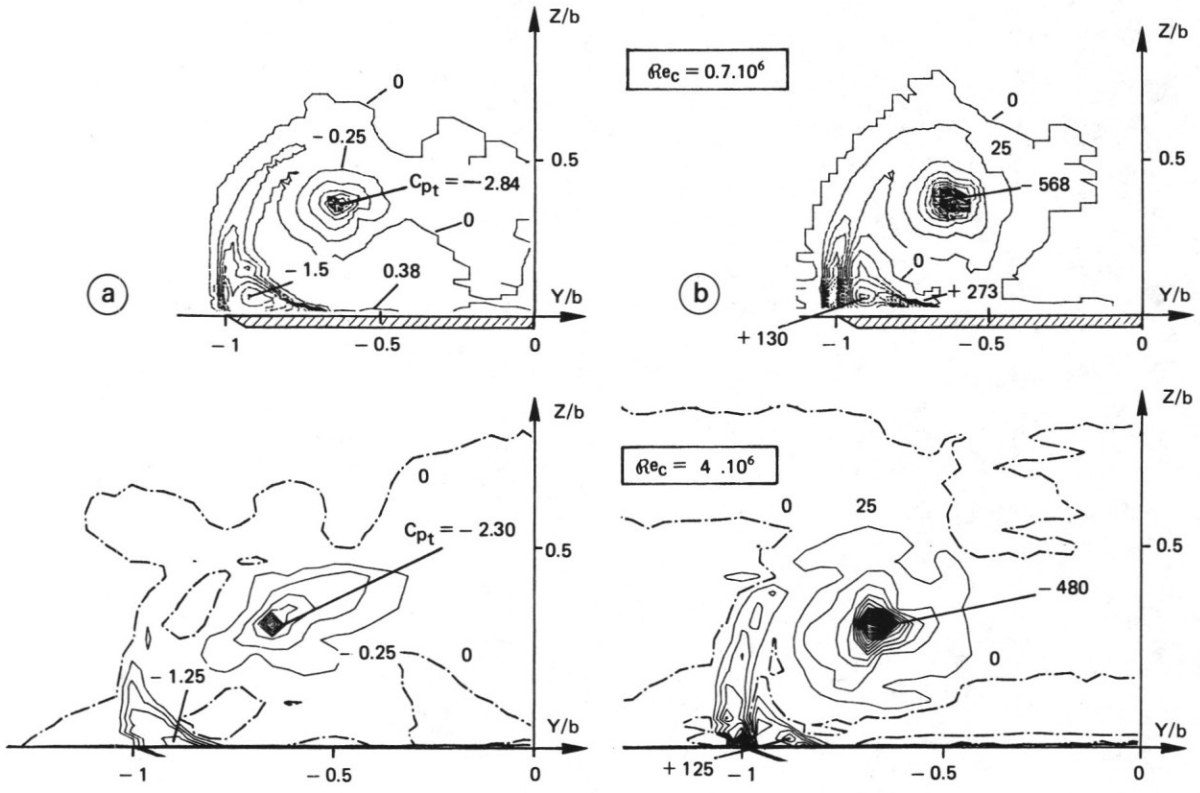

Figure 10. Flowfield in a vertical plane x/c ≃ 0.6 : a) Total pressure contours, $\Delta C_{p_t} = 0.25$, *b) Streamwise vorticity component contours* $\Delta\Omega_X = 25$.

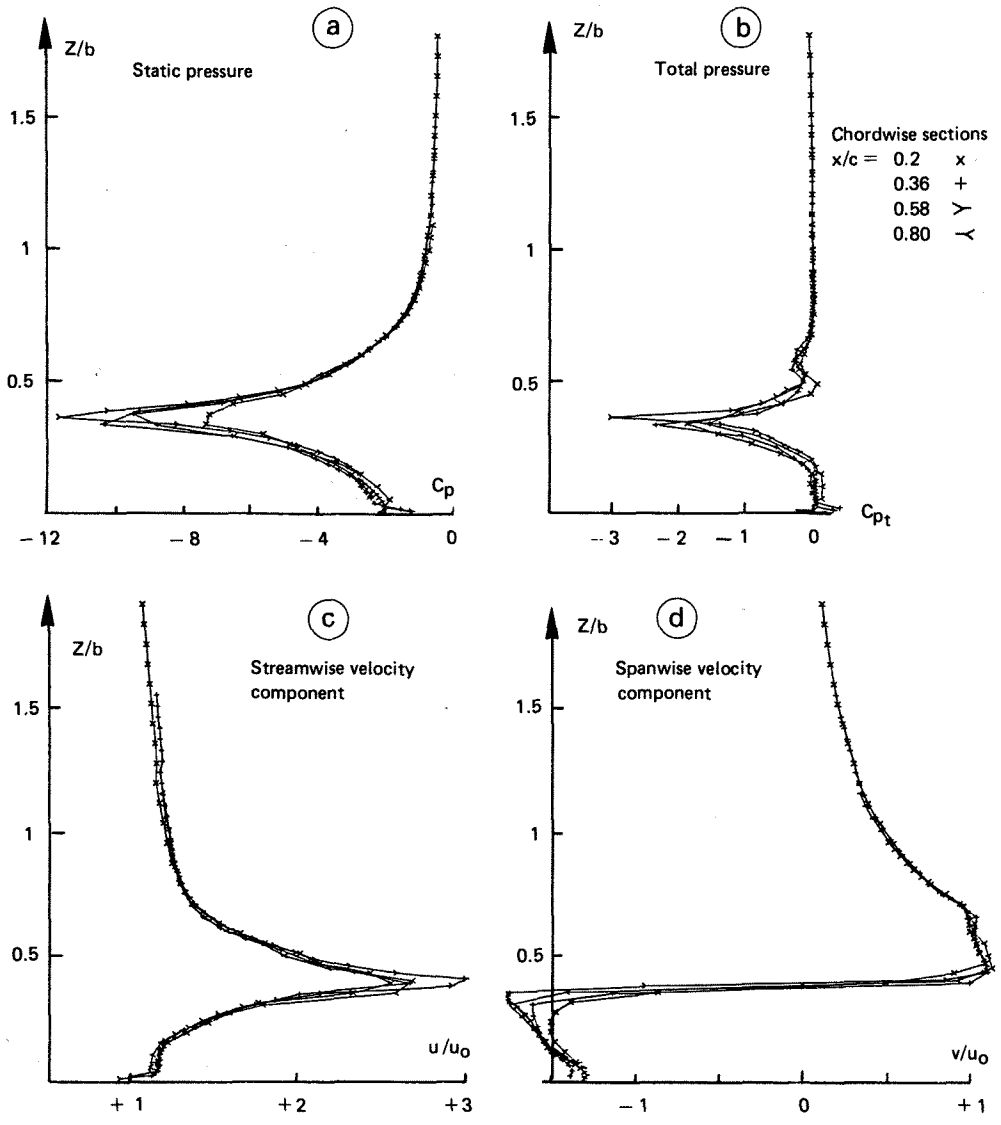

Figure 11. Corrected pressure and velocity profiles through vortex core, $Re_c = 0.7\ 10^6$, $\alpha = 20°$.

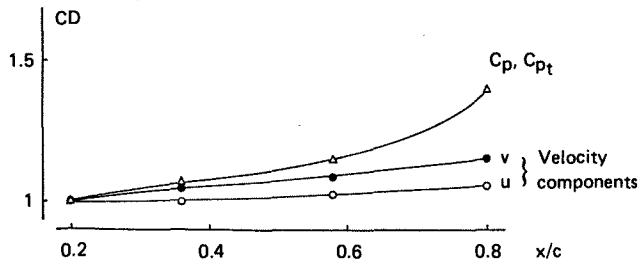

Figure 12. Chordwise variation of the conical dilatation coefficient CD, $\alpha = 20°$, $Re_c = 0.7\ 10^6$.

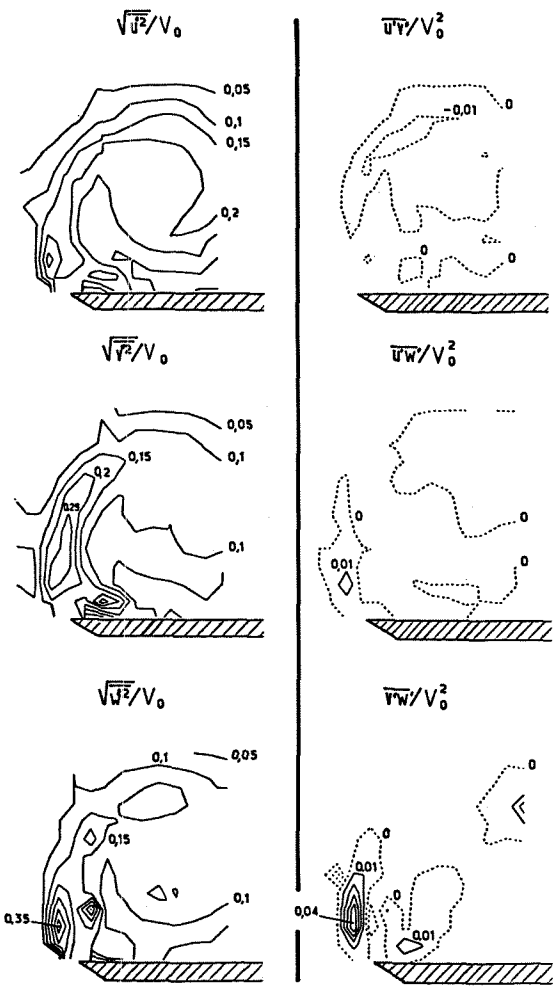

Figure 13. (Left) RMS values of velocity component fluctuations in a vertical plane, $\alpha = 20°$, $Re_c = 0.7\ 10^6$, $x/c = 0.6$.

Figure 14. (Right) Cross-correlation terms in a vertical plane, $\alpha = 20°$, $Re_c = 0.7\ 10^6$, $x/c = 0.6$.

Figure 14 displays the distributions of the normalized correlation terms $\overline{uv}/V_0^2$, $\overline{uw}/V_0^2$ and $\overline{vw}/V_0^2$. The $\overline{vw}$ term takes on large values in the region of the leading edge vortex sheet. They characterize the important shearing stresses which exist in a zone embedded between the leading edge vortex sheet and the secondary vortex.

III. Computation of Vortex Flow over Delta Wings

III.1. The Three-Dimensional Vortex Particle Method

The theoretical background and the numerical implementation of this time-accurate, unsteady method developed by Rehbach are reported in some detail in references(18, 19). We shall only recall its main features here.

1) The thin lifting surface (S) is discretized by plane panels using a doublet distribution of constant strength (μ) on each panel. The slip condition on (S) determines (μ).

2) Incompressible, inviscid flow in the computational domain (D) surrounding (S) is assumed, and it is described in terms of vorticity distribution :

$$\bar{\omega} = \nabla \times \bar{V} \qquad (1)$$

($\bar{V}$: velocity vector).

3) The vortex shedding mechanism follows from Kutta condition-type considerations, leading to the time discretization of the convection equation for the doublet strength of edge panels.

4) The time dependent evolution of vorticity-loaded particles that are shed at each time step into (D) from the edges of (S) is governed by the Helmholtz equation :

$$\frac{D\bar{\omega}}{Dt} = (\bar{\omega}.\nabla)\ \bar{V} \qquad (2)$$

5) The local velocity in the entire flow-field due to the influence of (S) and the vortex particles can be expressed employing Green's identity :

$$\bar{V} = \bar{V}_o + \frac{1}{4\pi} \iiint_D \left(\overrightarrow{\text{grad}}\ \frac{1}{r}\right) \times \bar{\omega}\, d\delta + \frac{1}{4\pi} \iint_S \left(\overrightarrow{\text{grad}}\ \frac{1}{r}\right) \times (\bar{n} \times \bar{V})\, d\sigma \qquad (3)$$

where $r = |\bar{r}|$ and $\bar{n}$ is the outward unit normal to the surface element $d\sigma$. The vorticity particles are convected away with the local velocity given by (3). Their position and vorticity at each time step are calculated using predictor-corrector schemes.

The prediction of the shed vorticity vector $\bar{\omega}$ requires a finite difference computation of $\nabla\mu$ on each panel : this computation entails the construction of a fine and regularly panelled grid, especially near the emission points. In Figure 15, the first grid shown displays rather large panels at the leading edge ; their skewness precludes an accurate computation of $\nabla\mu$, especially for low sweep angles. In addition, this grid features a certain number of triangular panels that lead to an overvaluation of velocity : disturbances consequently appear in the development of the streak-lines, as evidenced in Figure 15.a. On the contrary, a conical grid featuring panels of constant aspect ratio ($\frac{l}{L} = 0.5$) allows smoother development of the streak-lines (Figure 15.b). In addition, the computation converges faster. The corresponding streamlines have been computed using the computed, converged velocity field and a small pseudo-time step that gives remarkably continuous curves (Figure 15.c).

All the computational results presented in this paper were obtained using a conical grid ; initial data and conditins are defined as follows :

- the time step used for the unsteady calculation, Δt, corresponds to $V_o\ \Delta t$ equals the mean spacing between adjacent emission points,

and the calculation of shed vorticity does not associate more than three panels per streakline ;

- the initial vorticity vector at a leading edge emission point is constrained to lie in the wing plane, in the direction given by $\varepsilon = \frac{1}{2}(\frac{\pi}{2} - \phi)$, i.e., the apex semi-angle ; this choice of ε follows from experimental observations. The high sweep of the leading edge imposes the use of this rather arbitrary constraint ; it is not needed at the trailing edge emission points. Singularities in the velocity field resulting from the use of point vortices are smoothed out using a parabolic velocity profile within a pseudo-viscous radius R_V.

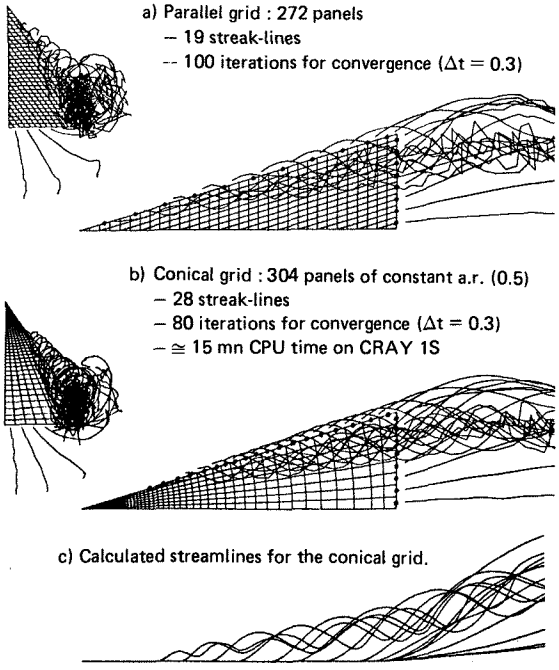

Figure 15. Computation of the vortex flow over the 75°-swept delta wing, α = 20°.

Tests have been performed by varying the parameters R_V and ε that did not affect the computational results. Similar tests were performed to validate the following procedures, that allow a significant reduction in computational time : particles that come too close together are merged into a single particle, and the remaining particles are progressively dissipated once they have reached a half wing chord downstream of the trailing edge.

The present computer code has been partially vectorized : each (ϕ, α) delta wing configuration computed using a conical grid (304 panels) and a time step $\Delta t = 0.3$ requires about 15 mn of CPU time on a CRAY 1S computer to achieve a converged value of the normal force (within 1% of its steady component).

III.2. Computational Results Compared with Experiment

A typical result for the present method is the time-dependent normal force curve $C_N = f$ (Iter or T = Iter x Δt) which is presented in Figure 16 for the 75°-swept delta wing at an angle of attack $\alpha = 20°$.

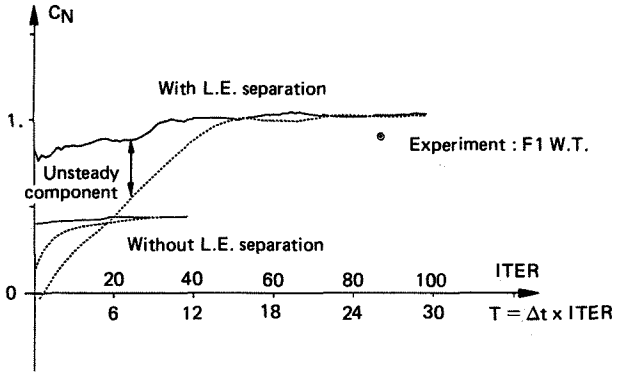

Figure 16. Convergence history for the computed normal force, α = 20°.

Shedding vortex particles from the trailing edge only leads to fast convergence towards the potential normal force value, that agrees well with a lifting surface solution (Figure 22).

With L.E. and T.E. vortex shedding, the same regular behaviour towards convergence as in the potential case is observed, the unsteady component of the normal force vanishing at $C_N \simeq 1$; this result, as well as the experimental value $C_N \simeq 0.9$ are obtained by integration of the pressure distributions. The experimental value does not include the non-zero lift at $\alpha = 0°$ ($C_{N_o} \simeq 0.07$), that is due to the beveledged lower surface of the wing.

The comparison between experimental and computed static pressure distributions is displayed in Figure 17 for three chordwise stations. At the $\frac{x}{c} = 0.52$ station, measurements from a probe survey close to the upper surface ($\frac{z}{c} \simeq 0.002$) agree with the pressure hole measurements ; however, the latter revealed pressure variations ($\Delta c_p/c_p \simeq 0.05$) that were induced by the exploring device interfering with the flowfield.

The use of the local spanwise coordinate $\frac{y}{b}$ emphasizes the non-conical features of the flow ; the same trends appear both in the experimental and computational results : the chordwise increase in upper surface static pressure as well as the inboard shift along the chord of the vortex axis location (which corresponds to the suction peak).

As compared to experiment, the computed spanwise location of the vortex axis is too close to the leading edge : this is mainly due to the part-span position of the first emission point downstream of the apex.

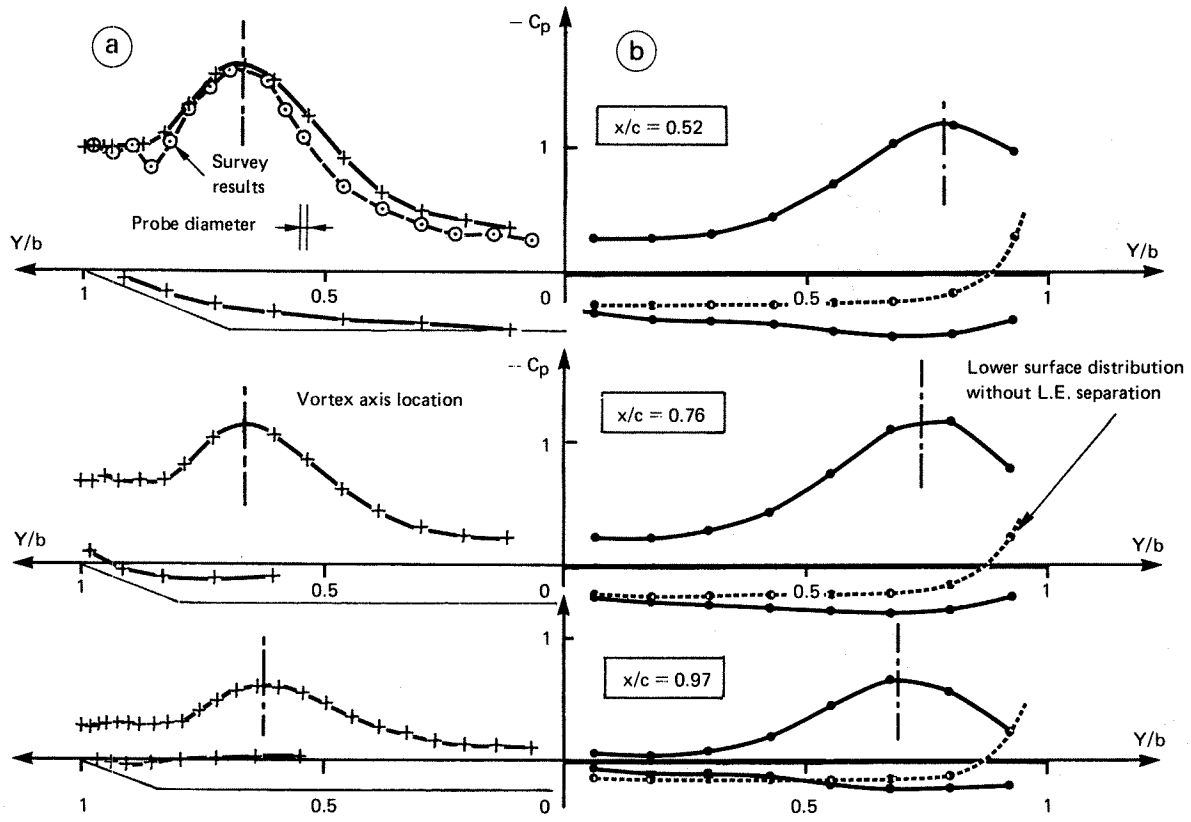

Figure 17. Static pressure distributions : a) Experiment : F1 W.T. $C_N \simeq 0.9$, b) Present method $C_N \simeq 1.0$.

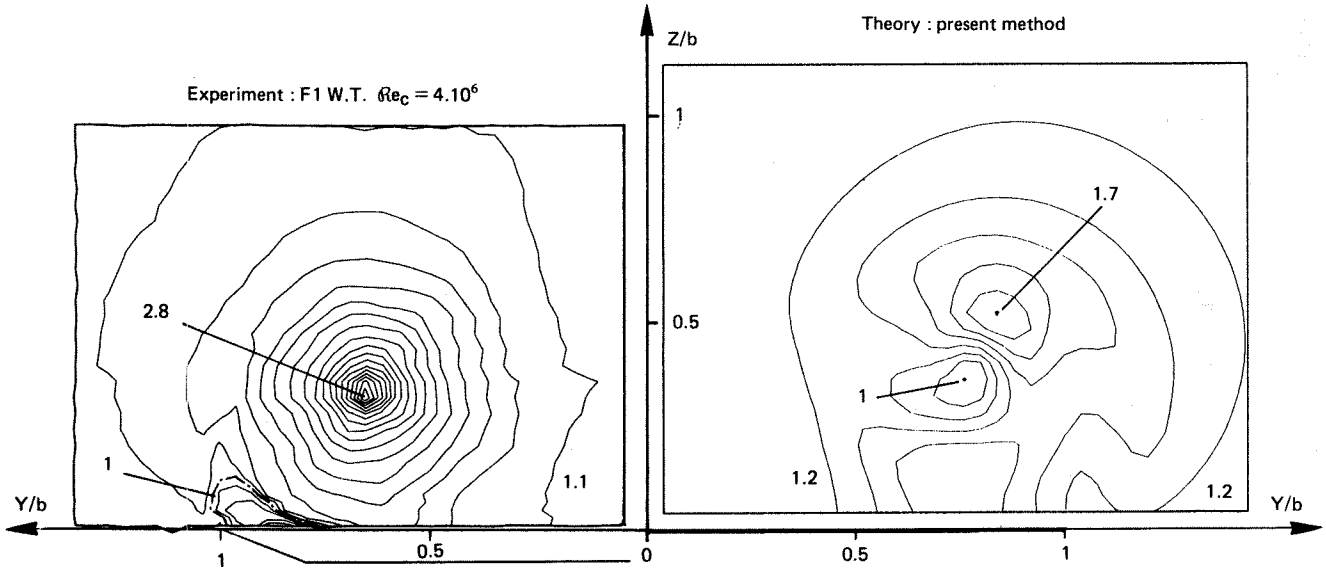

Figure 18. Velocity magnitude contours in the x/c = 0.8 plane, $\alpha = 20°$, $\Delta V/V_o = 0.1$.

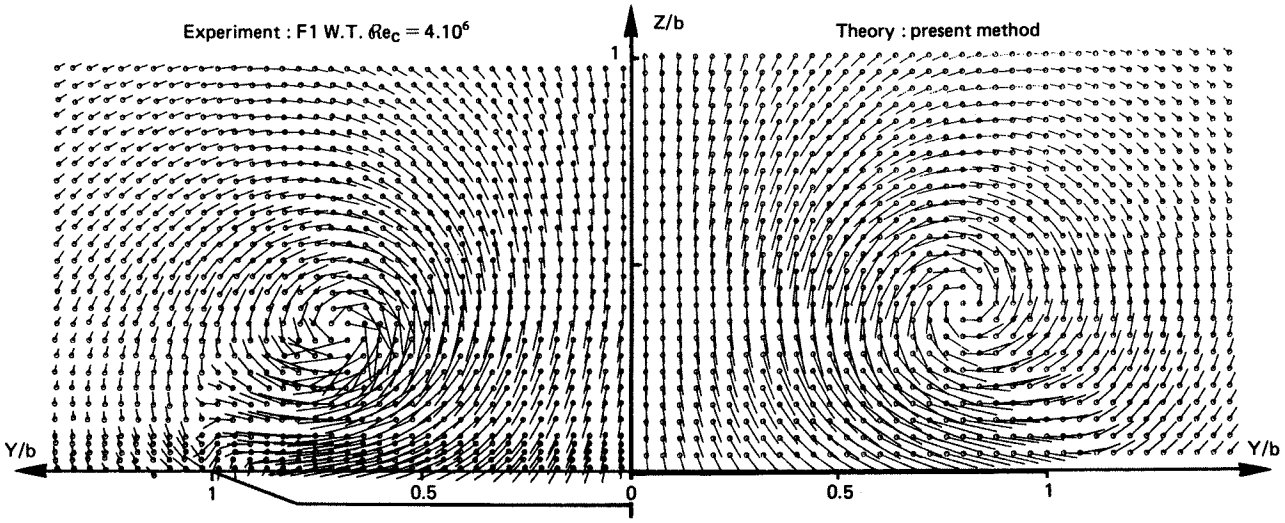

Figure 19. Planar view of the velocity vector field, x/c = 0.8, α = 20°.

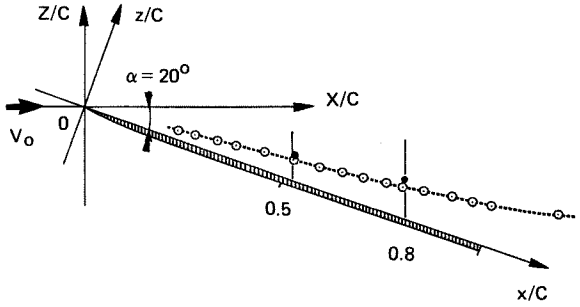

Figure 20. Vortex core location, α = 20° :
Experiment : ---⊙--- F1 W.T. surveys $Re_c = 4\ 10^6$
Theory : • Present method.

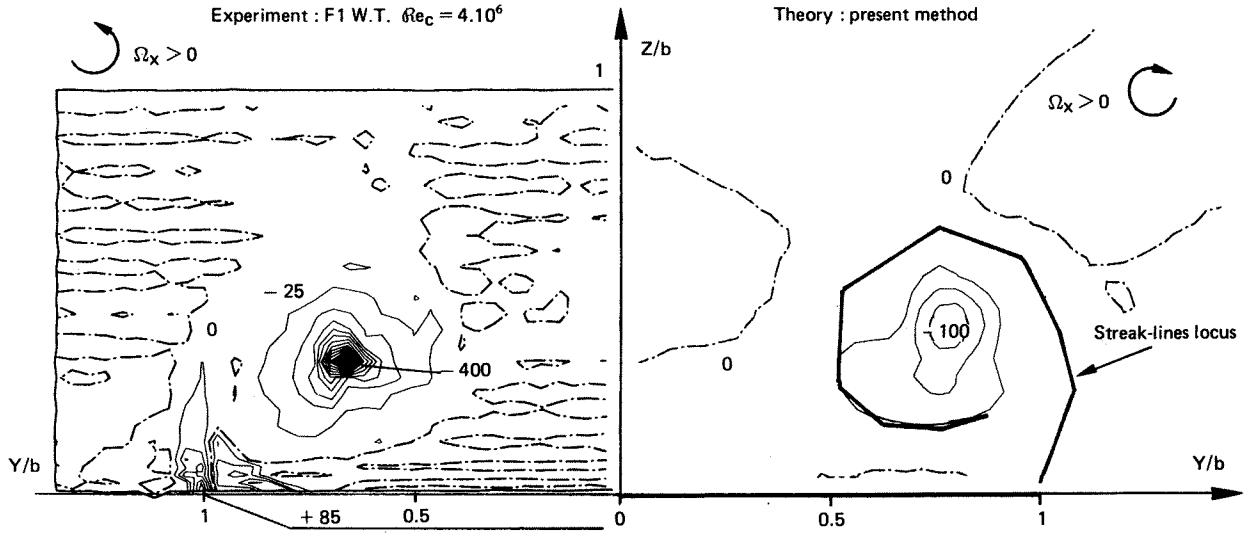

Figure 21. Streamwise vorticity component contours ($\Delta\Omega_X$ = 25.) in the x/c = 0.8 plane, α = 20°.

At each chordwise station, the present method overvaluates the lower surface pressure distribution, especially near the leading edge, where the influence of the accumulation of vorticity particles is felt ; this influence is evidenced here by displaying the lower surface pressure distribution in the potential case.

As regards the structure of the vortical flowfield, Figure 18 presents experimental and computational velocity magnitude contours in a vertical plane at the $\frac{x}{c} = 0.8$ chordwise station. These curves agree only near the wing upper surface : this reflects the agreement between measured and computed upper surface pressure distributions. The secondary separation is not predicted by the present method.

The inner part of the computed vortex flow displays a significant undervaluation of velocity magnitude that is essentially due to an undervaluated streamwise velocity component. In Figure 19, the projection in a vertical plane of the computed velocity vector field is indeed similar to that of the experimental velocity field at the same chordwise station ; this allows us to locate the computed vortex axis ; its $\frac{Z}{c}$ location is presented in Figure 20 for two chordwise stations above the wing, along with experimental data.

Taking into account the rather good agreement of the computed transverse velocity field with experiment, an attempt to compute the streamwise vorticity component Ω_X leads to the contours displayed against experimental results in Figure 21 : computation significantly undervaluates Ω_X, but the global behaviour of the field is captured. On the same figure, the locus of the streak-lines is shown which corresponds to the main vortex dimensions above the wing : agreement with the corresponding experimental limit (defined by $\Omega_X \equiv 0$) is reasonable. Among the improvements of the method that are presently being considered, the regularization of the velocity field induced by the vortex particles, as suggested in reference (19), should lead to a quantitatively more accurate prediction of the vortex structure.

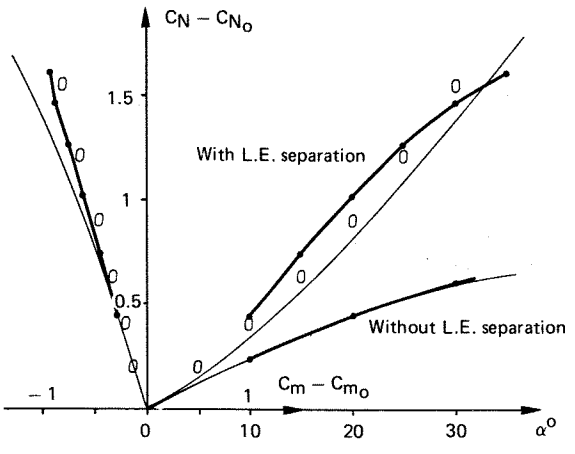

Figure 22. Normal force and pitching moment curves for the 75°-swept delta wing
Experiment : O Fl W.T., $Re_c = 4\ 10^6$
Theory : —— Lamar(20)
—●— Present method.

In order to demonstrate the capabilities of the present method, computations have been performed for several angles of attack up to $\alpha = 35°$ using the same initial conditions as for the $\alpha = 20°$ configuration. The corresponding $C_N(\alpha)$ and $C_m(C_N)$ curves are presented in Figure 22 : they are compared with the F1 wind tunnel test results and with computational results by Lamar(20). The good prediction of potential-type flow (without L.E. vortex shedding) by the vorticity particle method is confirmed both at $\alpha = 10°$ and 30°. As regards vortex flow, the present method predicts a realistic development of the normal force vs. α, considering that stall occurred at $\alpha \simeq 35°$ in the wind tunnel. The main features of the calculated vortex flowfields are displayed in Figure 23 by views of the streak-lines for $\alpha = 10°$ and 30°.

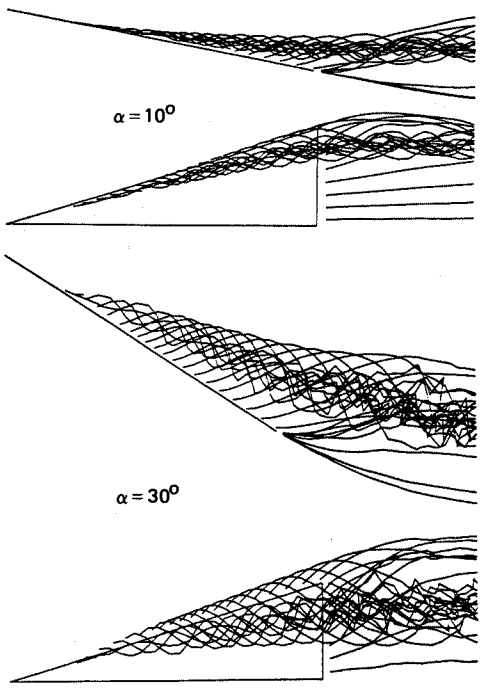

Figure 23. Computed streak-lines.

The applicability of the present method is further illustrated by the computation of vortex flow over a 70°-swept delta wing at $\alpha = 20°$ (still using the same initial conditions) ; the decrease in L.E. sweep leads to a conical grid comprising 504 panels (a.r. = 0.5). The grid is shown in Figure 24 along with computed streak-lines and streamlines. When comparing to the same representations of Figure 15, one expected sweep angle effect clearly appears : the vortex has moved closer to the leading edge. Concerning the flow structure, Figure 25 displays comparisons of our results with those obtained by Hoeijmakers and Rizzi(12), at the $\frac{x}{c} = 0.6$ chordwise station : we note a very good agreement of the upper surface pressure distributions. The extension of vortical flow regions above the wing and the general features of the vorticity field show a good agreement as well.

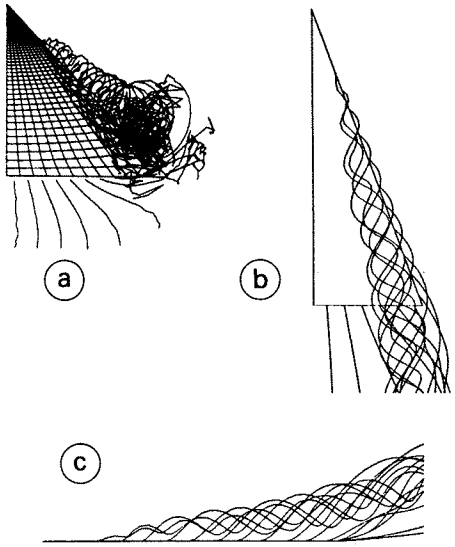

Figure 24. Present method : vortex flow over the 70°-swept delta wing, α = 20°. a) Rear view of the streak-lines development ; b) Calculated streamlines : upper view ; c) Calculated streamlines : transverse view.

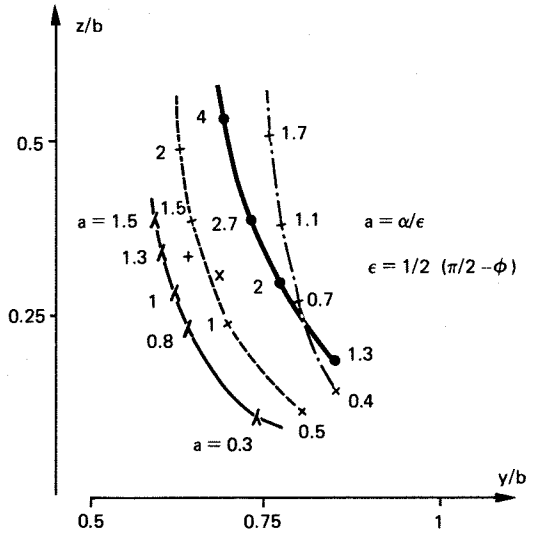

Figure 26. Vortex core location for delta wings :
Experiment + S2LCH W.T., Re_c = 0.7 10^6, x/c = 0.8, a = 2.7,
× F1 W.T., Re_c = 4 10^6, x/c = 0.8, a = 2.7
water tunnel, $Re_c \simeq 2\ 10^4$
Theory ---- Legendre(2)
-·-·- Smith(21)
—●— Present method x/c = 0.8.

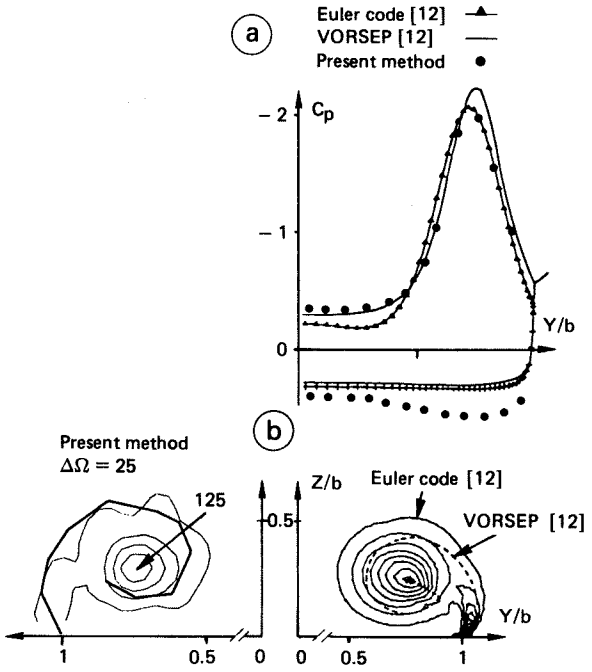

Figure 25. Computational results over the 70°-swept delta wing, α = 20°. a) Pressure distribution at x/c = 0.6 ; b) Vortex sheet position and vorticity magnitude contours.

Finally, Figure 26 presents a comparison of experimental and computational results concerning the vortex axis location above the wing. Experimental results clearly show a Reynolds number effect. The theoretical predictions of Legendre(2) and Smith(21) based on the assumption of conical flow are presented as reference. It is expected that the present method will yield results in better agreement with experimental results at high Reynolds number as soon as vortex shedding close to the apex has been improved on.

IV. Concluding remarks

In order to improve the knowledge of the vortex flow that occurs at the swept leading edges of slender wings, a fundamental investigation of the flow over a basic configuration -75°-swept delta wing, α = 20°- has been conducted at ONERA.

As expected, increasing the freestream Reynolds number from 1 10^6 to 4 10^6 causes strong changes in the upper surface boudary-layer, the mean transition location moving up towards the apex. Spatial flowfield visualizations using laser sheets evidence the slight effect of this large Reynolds number variation on the spatial location of the primary vortex. Furthermore, five-hole pressure probe surveys do not reveal any fundamental changes in the structure of the vortical flowfield over the entire range of freestream Reynolds numbers.

Otherwise, measurements reveal the non-conical nature of the vortex flow. Three-dimensional LDV measurements reveal a high turbulence level in the primary vortex core and leading edge vortex sheet, as well as the presence of large shear stresses in the zone embedded between the latter and the secondary vortex. These detailed results obviously emphasize the need for fine, non-intrusive experimental techniques, and provide a valuable reference data base for assessing three-dimensional computational methods devoted to the prediction of such complex flowfields.

It is thus seen that the vortex particle method yields an accurate representation of the chordwise evolution of upper surface pressure distributions. Lower surface pressure distribution are, however, significantly over-predicted. Inside the vortex, the computed streamwise velocity component is underpredicted, while the more accurate transverse velocity field enables us to compute the streamwise vorticity component. Otherwise, global features of the flow like the spatial extension of the primary vortex are correctly reproduced.

The capabilities of the method are demonstrated by its straightforward implementation for several different values of the angle of attack. The resulting $C_N(\alpha)$ and $C_m(C_N)$ curves are in good agreement with experiment. Finally, computation of the leading edge vortex flow over a 70°-swept delta wing at an angle of attack $\alpha = 20°$ using the present method leads to a remarkably good agreement with other methods (VORSEP, Euler code). Note that the present method does not require a spatial grid to compute the flowfield, nor an an initial guess of the leading edge vortex sheet location.

Further improvements of the vortex particle method are being considered, such as : a more accurate computation of lower surface pressure, an alternative numerical determination of $\nabla\mu$ allowing the use of non-structured grids that would allow a better discretization of the apex region, and a more sophisticated regularization model for the velocity field induced by the vortex particles. These improvements are to be included in extensions of the vorticity particle method presently being developed at ONERA to compute the vortex flow over wings of arbitrary thickness. They should eventually allow to simulate the secondary vortex.

Further analysis of the large amount of experimental data obtained on the 75°-swept delta wing model will provide essential informations to assess these computational methods.

References

1. Roy, M., "Caractères de l'écoulement autour d'une aile à flèche accentuée". Compte-rendus de l'Académie des Sciences T. 234 N° 26 (1952).

2. Legendre, R., "Ecoulement au voisinage de la pointe avant d'une aile à forte flèche aux incidences moyennes". La Recherche Aéronautique N° 30, 31, 35 (1952, 1953).

3. "High Angle of Attack Aerodynamics". AGARD C.P. 247.

4. "Aerodynamics of Vortical Type Flows in Three Dimensions". AGARD C.P. 342.

5. Werlé, H., "Etude physique des phénomènes tourbillonnaires au tunnel hydrodynamique". ATMA Communication (1961).

6. Hummel, D., "Experimentelle Untersuchung der Strömung auf der Saugseite eines schlanken Deltaflügels". Z. Flugwiss. 13, 1965, Heft 7.

7. Sforza, P.M. and Smorto, M.J., "Streamwise Development of the Flow Over a Delta Wing". AIAA Paper 80-0200.

8. Manie, F., Rehbach, C. and Schmitt, V., "Etude d'une aile à flèche variable en écoulement sub- ou transsonique". ICAS, Lisbon (1978).

9. Brocard, Y. and Manie, F., "Etude des caractéristiques de l'écoulement tourbillonnaire sur une aile en flèche". L'Aéronautique et l'Astronautique N° 82 (1980).

10. Manie, F., Néron, M., Schmitt, V., "Experimental and Computational Investigation of the Vortex Flow Over a Swept Wing". ICAS, Toulouse (1984). ONERA T.P. No 1984-3.

11. Cantaloube, B. and Huberson, S., "A New Approach Using the Vortex Point Method for Prediction of Rotor Performance in Hover and Forward Flight". 9th European Helicopter Forum, Stresa (1983).

12. Hoeijmakers, H.W.M. and Rizzi, A., "Vortex Fitted Potential Solution Compared with Vortex-Captured Euler Solution for Delta Wing with Leading Edge Vortex Separation". AIAA Paper 84-2144.

13. Brocard, Y. and Desplas, Ph., "Méthodes d'exploration des écoulements tourbillonnaires développées pour la soufflerie F1". AGARD C.P. 348 (1984).

14. Broussaud, P., "Dispositif pour l'étude détaillée de l'écoulement autour de grandes maquettes en soufflerie". 60th S.T.A. Meeting, Williamsburg (1983).

15. Afchain, D., Broussaud, P., Frugier, M. et Rancarini, G., "La soufflerie F2 du centre du Fauga-Mauzac". 20ème Colloque d'Aérodynamique Appliquée AAAF, Toulouse (1983). ONERA T.P. N° 1983-139

16. Boutier, A., D'humières, Ch. and Soulevant, D., "Three-Dimensional Laser Velocimetry : a Review". 2nd International Symposium on "Applications of Laser Anemometry to Fluid Mechanics", Lisbon (1984). ONERA T.P. No 1984-43.

17. Peake, D.J. and Tobak, M., "Three-dimensional Interactions and Vortical Flows with Emphasis on High Speeds". AGARDograph No 252.

18. Rehbach, C., "Numerical Calculation of Three-Dimensional Unsteady Flows with Vortex Sheets". AIAA Paper 78-111.

19. Morchoisne, Y., "Calcul d'écoulements instationnaires par la méthode des tourbillons ponctuels". AGARD-FDP, "Applications of CFD in Aeronautics", Aix-en-Provence (1986).

20. Lamar, J.E. and Gloss, B.B., "Subsonic Aerodynamic Characteristics of Interacting Lifting Surfaces with Separated Flow around Sharp Edges Predicted by a Vortex Lattice Method". NASA TN-D 7921 (1975).

21. Smith, J.H.B., "Improved Calculations of Leading Edge Separation from Slender, Thin Delta Wings". Proc. Roy. Soc., London, Series A 306 (1968).